Investigation of Slagging Characteristics in a 300 kW Test Furnace: Effect of Deposition Surface Temperature

5 **AUTHORS**, INCLUDING:

Hao Zhou

Zhejiang University

137 PUBLICATIONS   **799** CITATIONS

Investigation of Slagging Characteristics in a 300 kW Test Furnace: Effect of Deposition Surface Temperature

Hao Zhou,* Bin Zhou, Hailong Zhang, Letian Li, and Kefa Cen

Institute for Thermal Power Engineering, State Key Laboratory of Clean Energy Utilization, Zhejiang University, Hangzhou 310027, Zhejiang, P. R. China

ABSTRACT: The aim of this work is to evaluate the effect of deposition surface temperature on the characteristics of slagging deposit through a digital image technique. For this purpose, three slagging tests were carried out in a pilot scale furnace. An oil-cooled probe was used to collect the slags which formed at about 1523 K. The corresponding probe surface temperatures were in the ranges of 758−617, 693−597, and 669−560 K with deposit growth. The results show that the deposition surface temperature has an evident effect on the deposition rates and morphology. The stable thickness of deposit decreases with the increasing deposition surface temperature. The electron micrographs reveal that the higher deposition surface temperature results in the occurrence of a more compact morphology and more macro pores in the slag layer. Furthermore, the low deposition surface temperature can facilitate the formation of sulfates in the initial layer.

INTRODUCTION

Coal-fired power generation will continue to be the primary source of electric power in the next decades in China because of China's large coal reserves. Nevertheless, several inorganic constituents exist in coal in various forms. This will give rise to serious environmental and operational problems during coal combustion in power plant boilers.[1] Ash-related deposition problems are a vital concern issue for coal-fired boilers.[2] The deposits not only deteriorate the heat transfer of the overall system but also give rise to erosion of heat-exchanger tubes and unscheduled shutdown.[3,4] All these phenomena may cause a decrease in generating capacity, efficiency, and reliability of the system and an increase in cost of power generation.[5−9]

It is well-known that ash deposition is a complex combination of many physical and chemical processes. Ash deposit formation primarily depends on coal type, ash transport mechanisms, furnace temperature, surface temperature of boiler tube, materials of the tube, reaction atmosphere, flow field in the furnace, and so forth.[10]

It is generally acknowledged that inorganic constituents of coal will end up with fly ash during coal combustion. Zbogar et al.[11] demonstrated that ash species deposit on boiler tubes from the flue gas mainly through three transport mechanisms: diffusion, thermophoresis, and inertial impaction. According to Tomeczek et al.,[12] thermophoresis is the primary transport mechanism for submicrometer particles (<1 μm) to adhere to boiler tube; fine particles (<10 μm) are principally controlled by turbulent diffusion to stick to the tube surface; for large particles (>10 μm), inertial impaction is the most important transport mechanism.

In recent years, much research with respect to ash deposit characteristics have been carried out experimentally and theoretically. For the theoretical studies, Tomeczek et al.[12] developed a two-dimensional model to simulate the ash deposit formation on platen superheaters in PF boilers. A multiphase−multilayer flow and phase transformation model has been proposed by Ni et al.[13] to investigate the slag flow in a slagging entrained-flow gasifier. Waclawiak et al.[14] also used a 2D model to study the formation of the powdery, medium-temperature deposits on superheater tubes. Rushdi et al.[15] predicted the ash deposition behavior and evaluated the ash deposition tendency by a mechanistic approach. Even so, it is difficult to accurately simulate the deposit process of ash deposits because of the great number of physical and chemical processes involved. In consequence, it is very important to precisely monitor ash deposit growth online through digital image techniques.

For the experimental research, Wang et al.[16] evaluated the role of sulfate on biomass ash deposit formation on heat exchanger surfaces. Shimogori et al.[2] investigated the effect of alkali metals and fine ash particles on the decrease of heat transfer in the initial stage of ash deposition. Mu et al.[17] studied ash deposition behavior and the corresponding mineral transformation in an industrial-scale waste incineration plant. The inorganic component evolution of rubber has been determined by Alvarez et al.[18] during rubber tire combustion in a fluidized bed reactor. In addition, measuring the weight of deposit on the probe has been used to evaluate the influence of probe surface temperature on deposition rate.[19] Additionally, chemical equilibrium calculation was applied to obtain the fraction of molten slag in ash, and the results revealed that it correlated well with the experimental results.[20] Furthermore, an online weighing technique was used to measure the growth of ash deposits.[21] Even with these references, however, limited studies could observe the morphology of the ash deposit growth online and quantify the deposits with the development of a digital image technique, for instance, charge coupled device (CCD).

According to early research, the Na- and K-bearing compounds are key species contributing to the formation of the initial layer of ash deposits. The condensation of these alkali
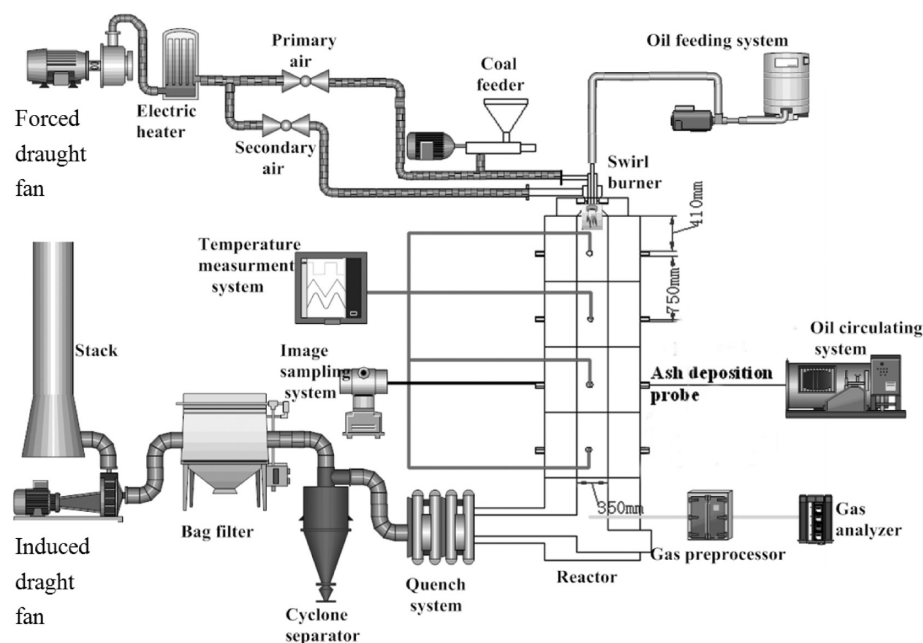
Figure 1. Schematic diagram of the pulverized coal combustion furnace.[22,23]

vapors on heat-exchanger surfaces is generally temperature-dependent. In consequence, it is of great interest to evaluate the effect of deposition surface temperature on ash deposit growth.

In our previous studies,[22,23] ash deposits were collected at only one deposition surface temperature. No tests have been carried out at other deposition surface temperatures. Therefore, the purpose of this study is to investigate the influence of deposition surface temperature on the deposit growth rate, deposit structure, and chemical composition. For this purpose, three slagging tests have been conducted in a pilot scale furnace by changing the inlet temperature of cooling oil (443, 493, and 543 K). By the evaluation of how the surface temperature of the deposition probe influences the deposit characteristics (growth rate, structure, and composition), an attempt is made to gain further insight into the formation mechanism of ash deposits.

2. EXPERIMENTAL SECTION

2.1. Pilot Plant Test Facility. The slagging tests were conducted in a pilot scale coal-fired furnace, as illustrated in Figure 1. It primarily consists of coal feeder, swirl burner, combustion chamber (inner diameter 350 mm; length 3950 mm), temperature measurement system, image sampling system, and ash deposition sampling system. To reduce heat loss during the experiments, refractory material is applied to mount into the interior of the combustion chamber. In this study, the coal feeding rate was fixed at 45 kg/h as the experimental condition reached the steady state.

During the experiments, an ash deposition probe made of stainless steel was used to collect the slagging deposits and inserted into the center of the furnace (see Figure 1). In addition, the image sampling system was developed to monitor the deposit growth online and was located in the opposite side from the ash deposition probe. During the experiments, the furnace temperatures were monitored by S-type thermocouples. The compositions of flue gas were analyzed by flue gas analyzer at the outlet of the furnace. Fine particles entrained by the flue gas were removed by the bag filter. The heat exchanger was applied to cool down the flue gas to around 400 °C before it

was discharged. Furthermore, the corresponding experimental conditions are given in Table 1.

Table 1. Experimental Conditions

	Zhun Dong coal
thermal load (kW)	300
excess air ratio	1.2
gas velocity (m/s)	~2.8
average furnace temperature around deposition probe (K)	~1523
oxygen concentration at the furnace outlet (%)	4.0−5.0
exposure time for ash deposition (min)	220

2.2. Deposit Sampling Technology. The ash deposition probe made of stainless steel is primarily composed of an oil-cooled tube section and a deposit sampling section (outer diameter 40 mm; length 70 mm), as shown in Figure 2a,b. A screw thread is used to connect them together. An oil-circulating temperature control unit is applied to maintain the inlet temperature of the cooling oil stable during the experiments. The maximum temperature of the cooling oil is 573 K according to the operating principle of the oil-circulating temperature control unit. Therefore, the inlet temperatures of the cooling oil were set as 443, 493, and 543 K for the three slagging tests. The corresponding outer surface temperature of the probe were in the ranges of 669−560, 693−597, and 758−617 K, respectively (see Figure 3). In this study, the deposition surface temperature corresponds to the outer surface temperature of the probe. In the following paragraph, 443, 493, and 543 K are denoted as the three different cases.

2.3. Deposit Image System and Principle of Digital Image Technique. A CCD monitoring system was applied to monitor the ash deposit growth online. The schematic diagram and detail of the system are exhibited in Figure 4a,b. The monitoring system is mainly composed of four parts: (1) camera lens, (2) protective tube, (3) CCD camera, and (4) camera shield. Detailed descriptions of the CCD monitoring system were presented in our previous studies.[22,23]

(a)

(b)

(c)
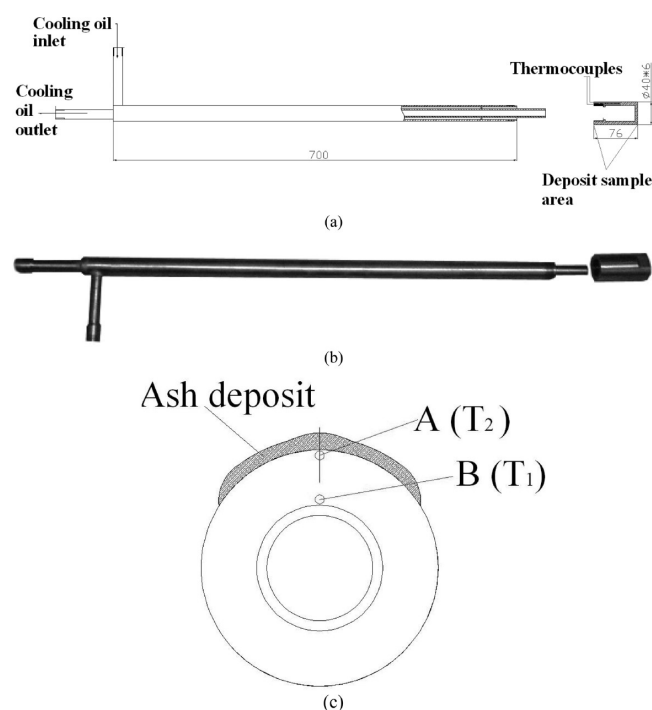
Figure 2. (a) Schematic diagram of deposition probe. (b) Deposition sampling part detail. (c) Close-up of the deposition sampling part.[22,23]
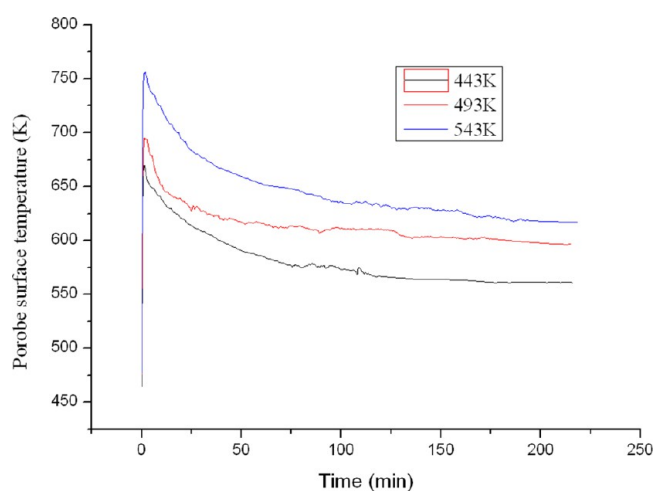
Figure 3. Surface temperatures of the deposition probe for different cooling oil temperatures.

The process of ash deposit growth is recorded by CCD camera as a video during the experiments. Subsequently, 24-bit images were obtained from the recorded video by the image processing system based on Matlab and its tool box. The slagging images undergo edge detection processing. Meanwhile, the Hough transform algorithm was applied to calculate the radius and center of the circle in the edge image, as depicted in Figure 5. In this study, the average height of ash deposit represents the thickness of deposit, and it is denoted by h. The outer diameter of deposit probe D_1 is constant during the experiments. In addition, the pixel numbers of the diameter D_1 is denoted as P_D. P_h represents the pixel numbers of the deposit thickness. These two parameters can be easily calculated by the image processing system. In consequence, the deposit thickness h can be obtained by the following equation:
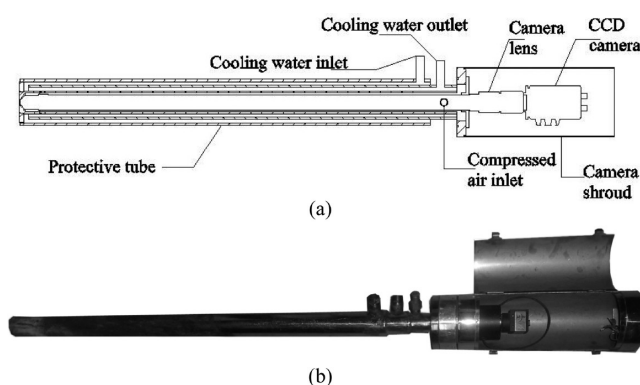
Figure 4. (a) CCD monitoring system. (b) CCD monitoring system detail.[22,23]

$$h = D_1 \cdot P_h / P_D \qquad (1)$$

2.4. Fuels. Zhun Dong (ZD) coal produced in Xinjiang province of China was selected as the feed coal during the experiments. The proximate analysis, ultimate analysis, calorific value, and ash fusion temperature of the feed coal are shown in Table 2. Moreover, Table 3 illustrates the chemical compositions of the coal ash. Obviously, it can be found that the feed coal ash has high level of sodium, which accounts for 9.32 wt % of the total sum. Furthermore, the coal was milled to 83.9 wt % less than 70 μm before the experiments. The corresponding particle size distribution of the pulverized coal measured by a Malvern particle size analyzer is illustrated in Figure 6.

2.5. Calculation of Heat Flux through the Deposition Probe. During the experiments, fly ash particles principally adhere on the upstream side of the probe. In consequence, the morphology of the deposit is analogous to a half-ellipse in shape (see Figure 2c). Therefore, the mathematical model of cylindrical wall heat conduction can be applied to determine the heat flux through the deposition probe. To simplify the calculation, the heat transfer is assumed to be one dimensional and in the direction of heat flux, which penetrates through point A to B in Figure 2c. Consequently, the heat flux through the probe can be obtained by the following equation:

$$q = \frac{\lambda(t_2 - t_1)}{r \ln\left(\frac{r_2}{r_1}\right)} \qquad (2)$$

where λ represents the thermal conductivity of deposition probe material; t_1 and t_2 are inner and outer surface temperatures of deposition probe, respectively; r is the radius of deposition probe; r_2 is the distance from point A to the center of the probe in Figure 2c; r_1 is the distance from point B to the center of the probe in Figure 2c.

3. RESULTS AND DISCUSSION

3.1. Visual Evaluation of the Slagging Deposits. The slagging deposits collected on the deposition probe for the three cases after an exposure time of 220 min are exhibited in Figure 7. The order of deposits for the three cases shown from left to right is 543, 493, and 443 K. Obviously, it can be seen that the color depth of deposit surface increases with the deposition surface temperature. This phenomenon can indicate that the sintering degree of three deposits increases with the deposition surface temperature.
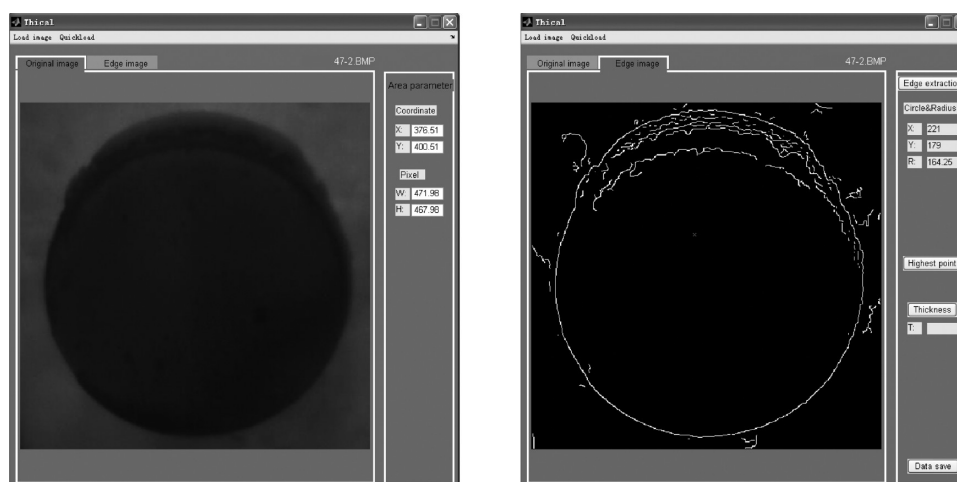
Figure 5. Detail of digital image processing; the original slagging image (left) and the edge image (right).

Table 2. Proximate Analysis, Ultimate Analysis, Ash Fusion Temperature, and Calorific Value of Feed Coal

		ZD coal
moisture (wt %, ad)		15.6
proximate (wt %, db)	volatile matter	32.79
	fixed carbon	52.91
	ash	12.3
ultimate analysis (wt %, db)	carbon	64.07
	hydrogen	3.58
	nitrogen	0.65
	sulfur	0.18
	oxygen	19.22
HV (M J/kg)	HHV	24.01
ash fusion temperature (°C)	IT	1213
	ST	1218
	HT	1221
	FT	1231

Figure 6. Size distribution of the ZD coal.

Figure 8 shows the cross-sectional structure of the three deposits. Apparently, it can be found that the three deposits appear to be similar layered structures with different colors and hardness. Along the deposit thickness direction (from inner to outer), the deposit is principally composed of three layers: layer 1 (the initial layer), layer 2 (the sintered layer), and layer 3 (the slag layer). The initial layer primarily consists of powdery, loosely bonded particles with no evident sintering. The sintered layer is characterized by serious sintering with a structure that is more dense than that of the initial layer, as illustrated in Figure 8. The slag layer is mostly molten with a hard structure. In this layer, the surface temperature of the deposit increases up to the melting temperature of the low-temperature melting eutectic point as the deposit grows further. The increase in surface temperature of the ash deposit will result in the softening and even melting of the deposit. Consequently, the slag layer presents a smooth and dense textured structure.

3.2. Growth of the Slagging Deposits. The frame rate of the CCD camera was set as 3 frames/s during the experiments, which leads to the produc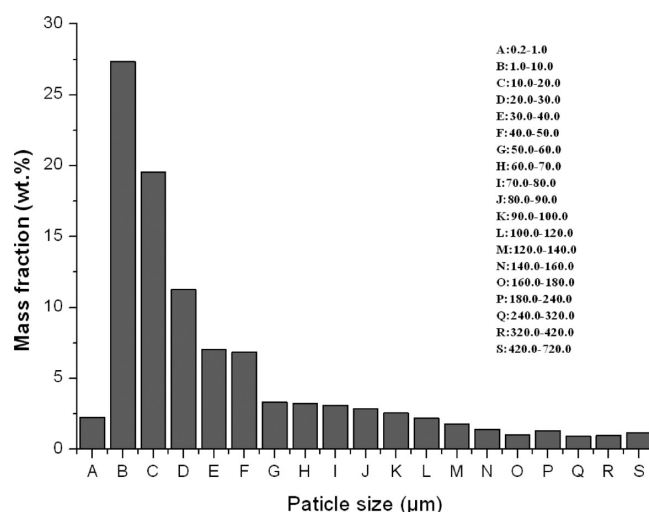tion of too many images. Thus, the digital image processing system is applied to extract one image per 5 min from the video to obtain the deposit thickness.

Figure 9 exhibits the variation of deposit thickness with time for the different deposition surface temperatures. An interesting observation can be made that the three deposits have a similar growth trend. In addition, it can be observed that all the curves in Figure 9 consist of four segments with different slopes. This result reveals that the growth process of the slagging deposits can be divided into four stages: stage 1 (stage$_{O-A}$), stage 2 (stage$_{A-B}$), stage 3 (stage$_{B-C}$), and stage 4 (stable stage). This phenomenon correlates well with the observations mentioned in section 3.1 that the three deposits all have three-layer structures. Additionally, it can be found that the deposits grow linearly with time in stage 1 with considerable growth rates. Subsequently, the deposit growth rates become moderate in stage 2. In stage 3, the deposit thickness still increases with time, but the growth rate further decreases. Finally, the deposit thickness fluctuates around a certain value and does not

Table 3. Chemical Compositions of Ash (Weight Percent)

Al$_2$O$_3$	CaO	Fe$_2$O$_3$	K$_2$O	MgO	MnO$_2$	Na$_2$O	P$_2$O$_5$	SiO$_2$	TiO$_2$
14.896	34.828	4.909	0.503	2.799	0.0186	9.319	0.0344	31.814	0.879
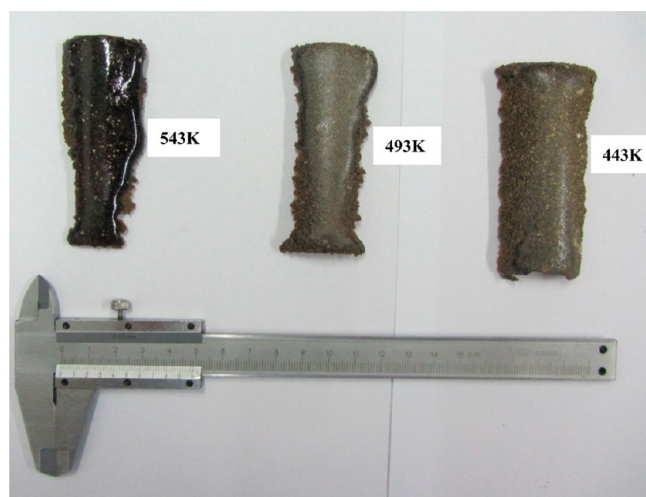
Figure 7. Photo of ash deposits from the probe with different surface temperatures.

Figure 9. Deposit thickness as a function of time for the different cases.

Figure 10. Heat flux through the deposit probe versus deposit thickness for the different deposition surface temperatures.

increase any more in stage 4, which implies that the deposit growth achieves the stable stage of slagging. This may result from the balance of viscous force, surface tension, and gravitational force acting upon the molten deposit surface.

Additionally, for the 443 K case, it can be observed that the rates of thickness increment in stages 1, 2, 3, and 4 are 0.069, 0.035, 0.011, and 0 mm/min (see Figure 9), respectively. Apparently, this result implies that the rate in stage 1 is significantly larger than those in stage 2 and stage 3, as shown Figure 9. In addition, stages 1, 2, and 3 last 20, 120, and 55 min, respectively. For the 493 K case, it can be seen that the rates of thickness increment in stages 1, 2, 3, and 4 are 0.048, 0.030, 0.007, and 0 mm/min, respectively. The corresponding durations of the first three stages are 25, 100, and 60 min, respectively. For the 543 K case, the rates of the deposit thickness increment for stages 1, 2, 3, and 4 are 0.032, 0.025, 0.011, and 0 mm/min, respectively. The corresponding durations of the first three stages are 30, 70, and 85 min, respectively.
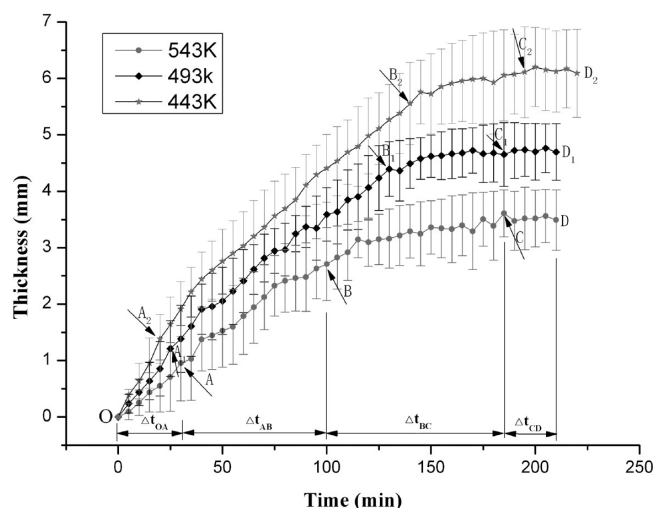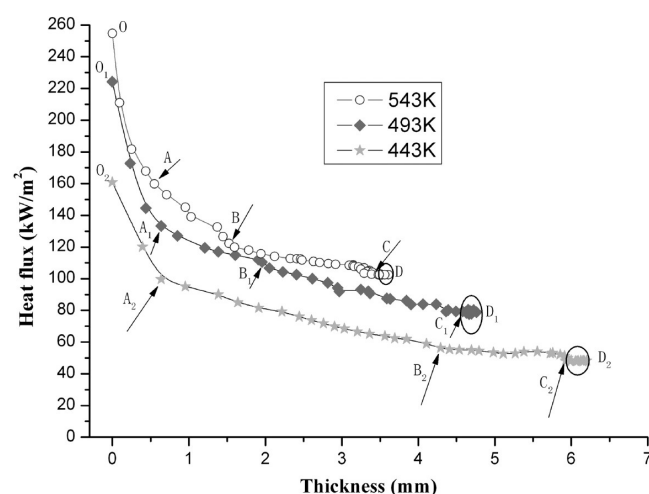

Figure 8. Cross sections of slags collected for different cases.

a. 443K

b. 493K

c. 543K
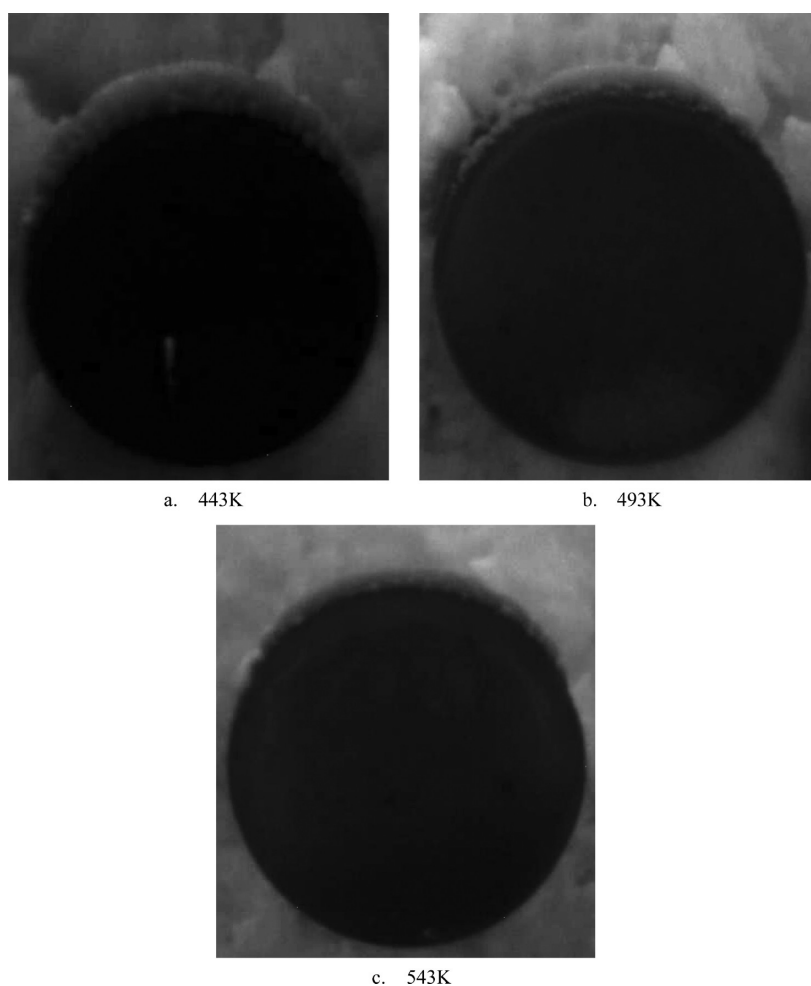
Figure 11. Morphology of the three deposits at stable stage from the CCD camera.
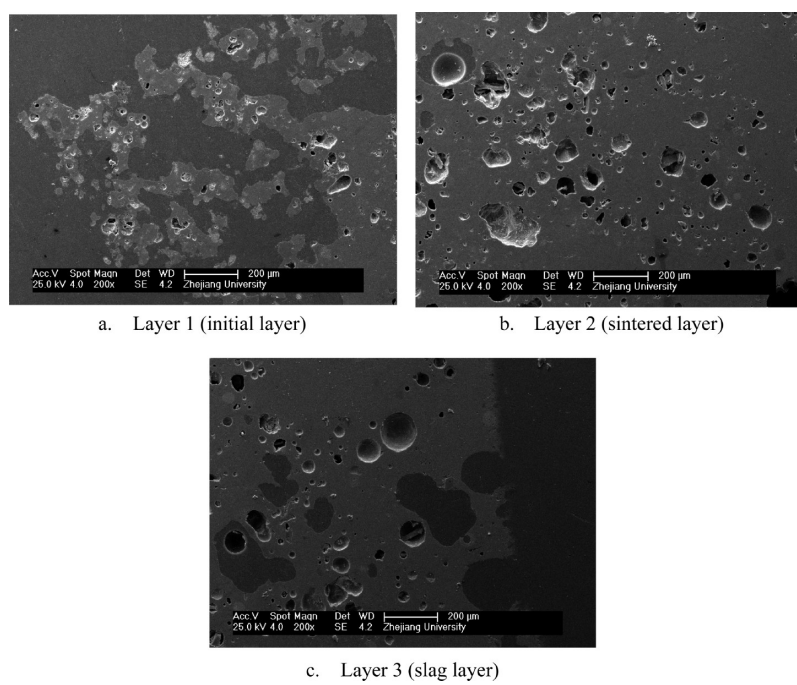
a. Layer 1 (initial layer)

b. Layer 2 (sintered layer)

c. Layer 3 (slag layer)

Figure 12. SEM photograhs of cross-sectional structures of each layer of the deposit for the 443 K case.

a. Layer 1 (initial layer)   b. Layer 2 (sintered layer)

c. Layer 3 (slag layer)

Figure 13. SEM photograhs of cross-sectional structures of each layer of the deposit for the 493 K case.

a. Layer 1 (initial layer)   b. Layer 2 (sintered layer)
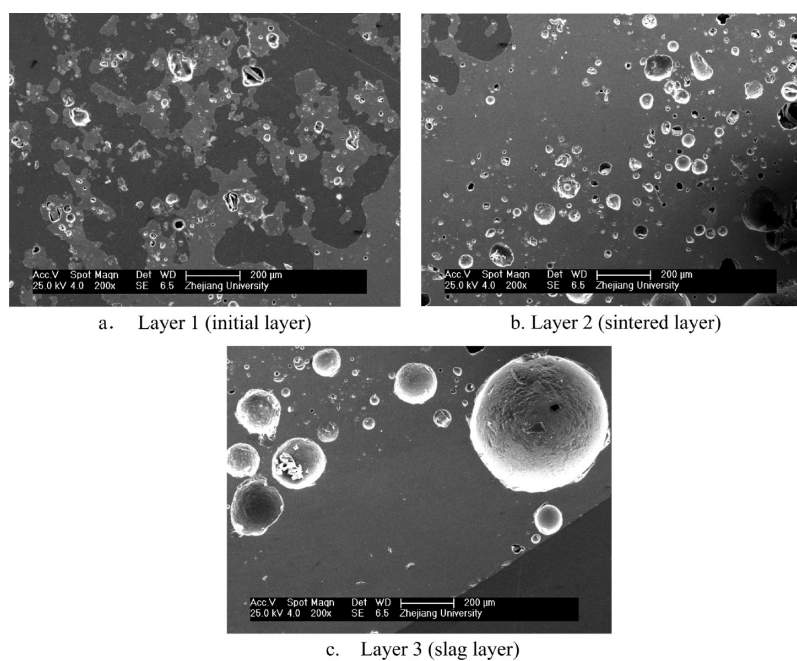

c. Layer 3 (slag layer)
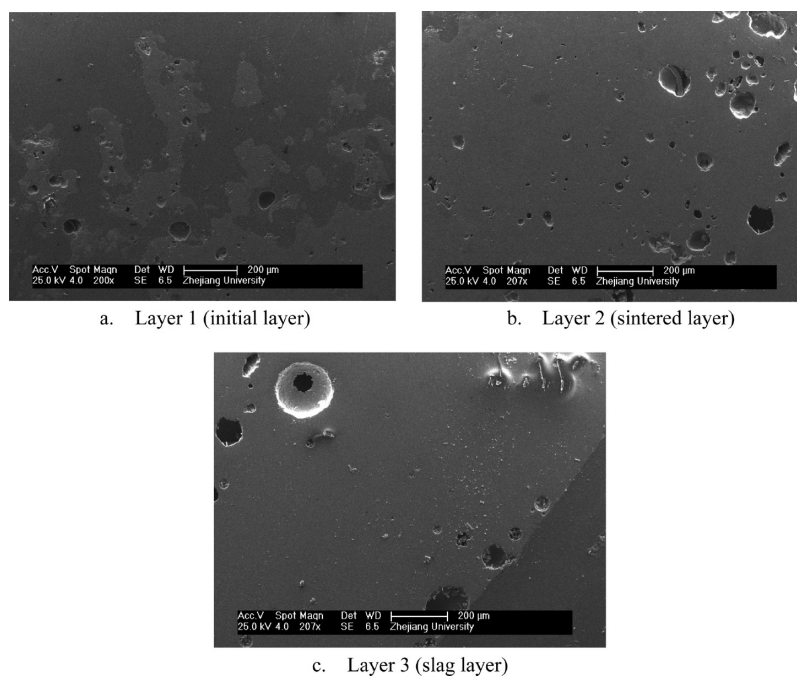
Figure 14. SEM photograhs of cross-sectional structures of each layer of the deposit for the 543 K case.

Table 4. Chemical Compositions of Ash Deposits Collected on Deposition Probe for the Three Cases Analyzed by SEM-EDX
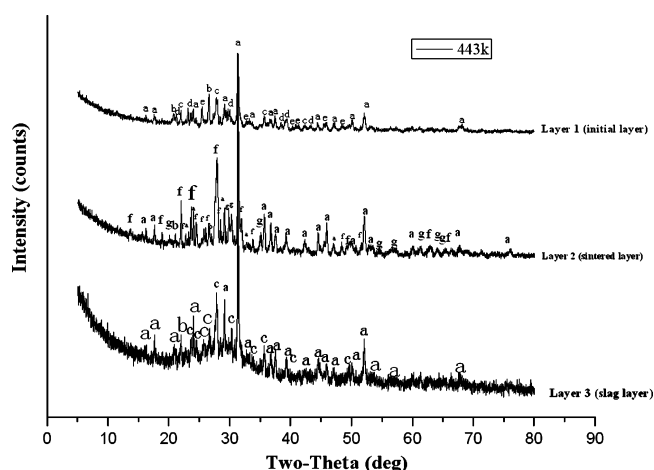
case		Na_2O	MgO	Al_2O_3	SiO_2	K_2O	CaO	SO_3	Fe_2O_3
443 K	layer 1	2.07	1.42	17.69	49.14	0.19	19.60	3.24	6.65
	layer 2	3.37	1.73	14.98	50.89	0.20	20.02	1.93	6.88
	layer 3	2.59	2.38	15.90	46.32	0.39	25.25	2.89	7.13
493 K	layer 1	2.37	1.83	16.94	46.43	0.19	24.61	2.41	5.23
	layer 2	2.11	1.75	14.43	46.77	0.18	26.68	1.64	6.46
	layer 3	2.56	1.81	16.78	48.8	0	21.28	2.10	6.64
543 K	layer 1	3.59	1.29	19.28	52.88	0.34	16.63	2.21	3.77
	layer 2	2.99	1.71	15.95	49.80	0.22	21.73	1.00	6.61
	layer 3	2.03	2.30	15.59	47.08	0.27	23.86	1.85	7.02
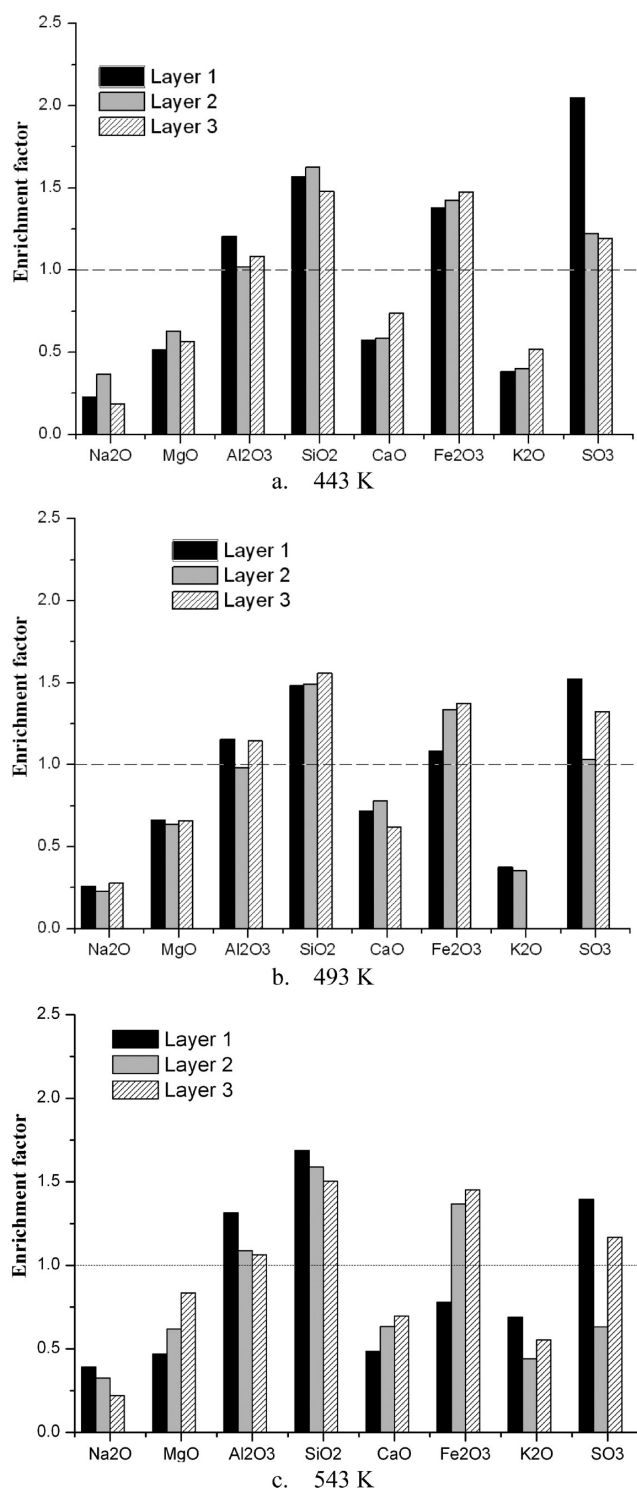
Figure 15. Enrichment factors of the ash deposit for the different deposition surface tempeartures.

Figure 16. X-ray diffraction analysis of the ash deposit collected for 443 K. (a: Gehlenite, syn-$Ca_2Al(AlSi)O_7$. b: Quartz-SiO_2. c: Bytownite-$Ca_{0.85}Na_{0.14}Al_{1.83}Si_{2.16}O_8$. d: Nepheline (Si-rich), syn-$Na_{6.8}Al_{6.3}Si_{9.7}O_{32}$. e: Armalcolite, syn, heated-$Fe_{0.5}Mg_{0.5}Ti_2O_5$. f: Anorthite sodian-$Na_{0.34}Ca_{0.66}Al_{1.66}Si_{2.34}O_8$. g: Diopside-$Mg_{0.6}Fe_{0.2}Al_{0.2}CaSi_{1.5}Al_{0.5}O_6$.)

Moreover, it should be noted that stage 1 (stage $_{O-A}$) in all three cases corresponds to the initial stage of the deposit formation. The deposit growth rate in this stage is largest during the deposit growth process for all three cases. It can be found that the rates of thickness increment for the three cases in the initial stage follow the order 443 K > 493 K > 543 K, as shown in Figure 9. Nevertheless, the corresponding duration of the initial stage presents the opposite tendency. In consequence, it can be concluded that low deposition surface

temperature can slightly facilitate the formation of the initial layer. As is well-known, alkali-containing component condensation is the precursor to the formation of the initial layer. First, the alkali-based vapors condense either homogeneously to form submicrometer-sized particles or heterogeneously on fly ash particles before deposition on the probe surface. The cohesive condensed vapor acts as glue, which promotes the Si—Ca-containing fly ash particles to stick to the deposit surface. The deposition surface temperature in the 443 K case is the lowest among the three cases. The low deposition surface temperature can facilitate the condensation of volatile inorganic components on the deposition probe. Thus, the deposition rate of the initial stage for the 443 K case is the largest among the three cases.

In addition, stages 2 and 3 for the three cases are typically referred to as the process of sintering. The deposition rates of stage 2 are triple to quadruple those of stage 3. Consequently, stages 2 and 3 can be distinguished into early stage and later stage sintering, respectively. The sintering process gives rise to increased contact area between the ash particles in a deposit. In addition, densification and shrinkage of ash particles will occur during the sintering process. Therefore, the deposition rates for stages 2 and 3 are significantly slower than that for stage 1. Stage 2 (early stage sintering) mainly involves chemical reaction sintering and solid-state sintering. The chemical sintering takes place between the particles and the gas phase components or between particles. This process will result in a formation of a third compound, and it will further cause the neck formation between the ash particles. In addition, the solid-state sintering is a slow sintering process with no melt involvement. In this process, densification takes place only when the material is transfered from the grain boundary between particles or from the particle volume. Stage 3 (later stage sintering) involves the occurrence of melt, shrinkage of pore structure, and pore filling by melt. Consequently, the deposition rates for stage 3 are dramatically less than those for stage 2. Meanwhile, the appearance of melt in this sintering process will give rise to the impacting of Si—Ca-containing fly ash particles adhering to the accumulated deposits. Moreover, the shrinkage of pores and viscous flow of melt will cause an
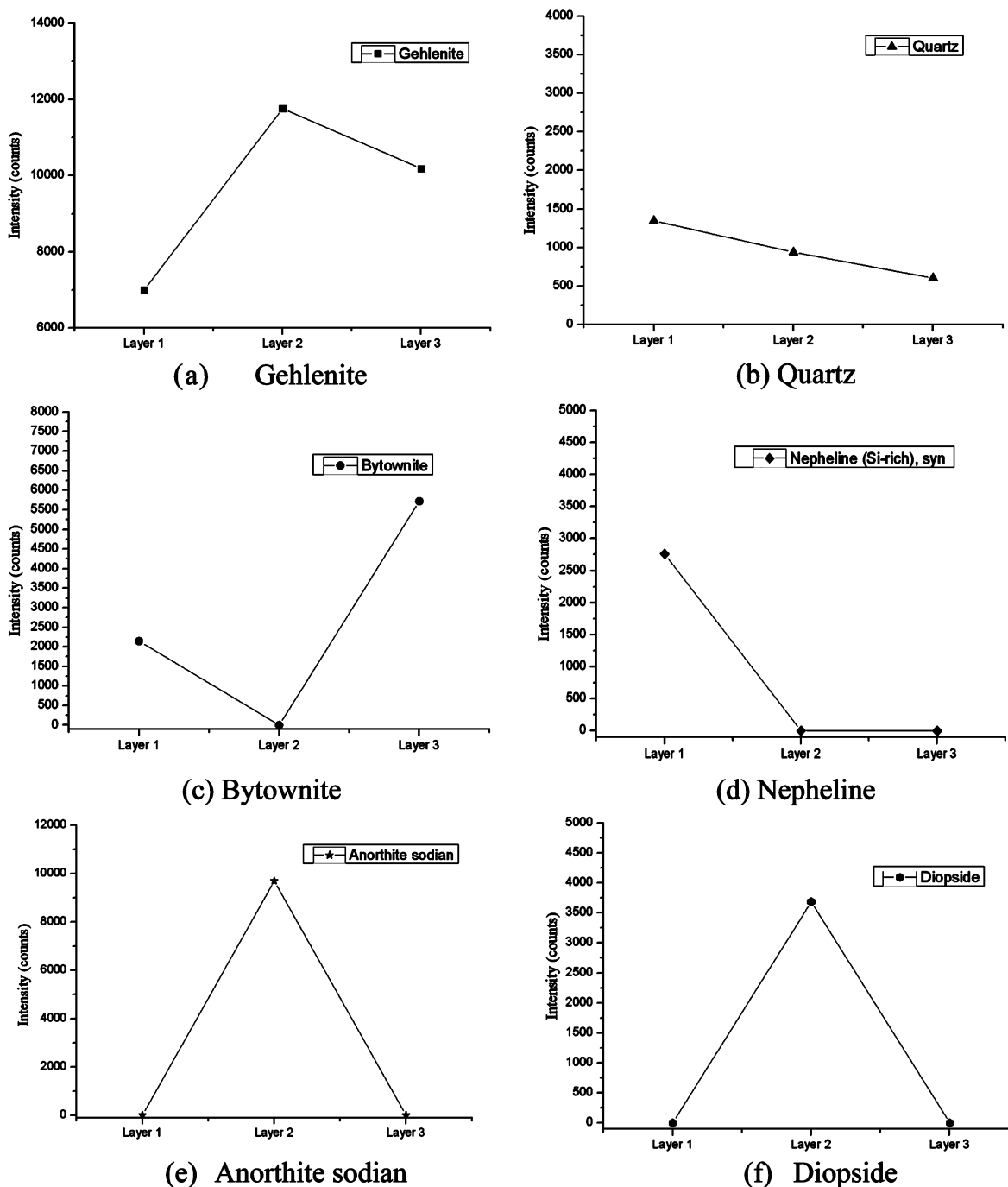
Figure 17. Changes to the main mineral phase of the deposit sample versus layer structure for the 443 K case.

evident increase in deposit strength. In consequence, the slag layer appears to have a more compact and dense morphology.

In addition, the variations of heat flux through the deposition probe with deposit thickness for the different deposition surface temperatures are shown in Figure 10. It can be seen that the heat flux decreases with the deposit growth. Considering Figures 9 and 10, the relationship between heat flux with time can be formulated into eqs 3−5 for the 543, 493, and 443 K cases, respectively.

$$q = 136.40773e^{-t/22.69731} + 105.86228 \qquad (3)$$

$$q_1 = 117.18405e^{-t/26.13578} + 82.06618 \qquad (4)$$

$$q_2 = 88.02761e^{-t/29.99832} + 51.32147 \qquad (5)$$

According to the attenuation rate of heat flux, the deposit growth also can be divided into four stages, as shown in Figure 10. It can be seen that the location of points A, B, C, and D in Figure 10 does not correspond to that in Figure 9. In addition, the heat fluxes decline significantly in stage 1(stage $_{O-A}$) for all the three cases. This stage corresponds to the initial layer of deposits. In general, the initial layer of deposit consists of loosely bonded, unconsolidated particles with no evident sintering, which appears as a particulate and porous structure, as mentioned in Section 3.1. Because the initial layer behaves as a large thermal resistance, heat flux obviously decreases as deposits increase. For the 543 K case, the duration of this stage
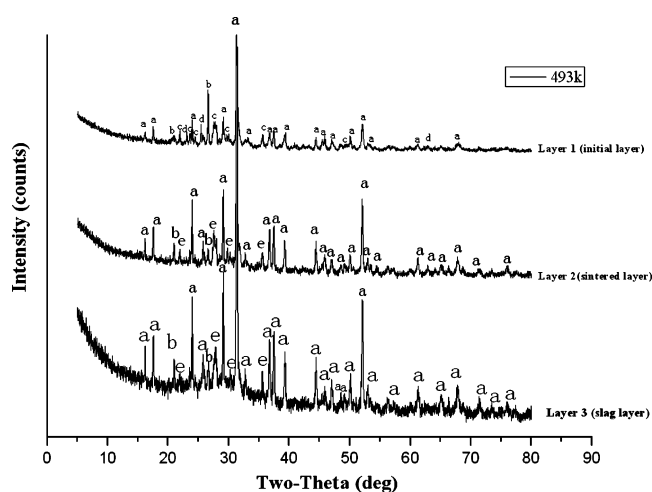
Figure 18. X-ray diffraction analysis of the ash deposit collected for 493 K. (a: Gehlenite-$Ca_2Al(AlSi)O_7$. b: SiO_2. c: Anorthite sodian-$Na_{0.34}Ca_{0.66}Al_{1.66}Si_{2.34}O_8$. d: Olivine-$Mg_{1.8}Fe_{0.2}SiO_4$. e: Bytownite-$Ca_{0.85}Na_{0.14}Al_{1.85}Si_{2.16}O_8$.)

is 20 min, and the corresponding thickness of this layer is 0.55 mm. Furthermore, the reduction of heat flux in this stage is 94.94 kW m^{-2}. For the 493 K case, this stage lasts 15 min, and the corresponding decrease in heat flux is 91.02 kW m^{-2}. The thickness of this layer is 0.64 mm for the 493 K case. However, this stage lasts only 10 min for the 443 K case. In addition, the thickness of this layer is 0.64 mm, and the corresponding
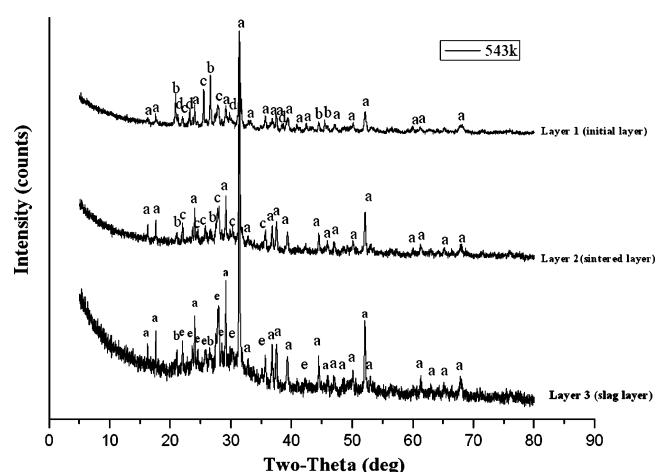
Figure 20. X-ray diffraction analysis of the ash deposit collected for 543 K. (a: Gehlenite-$Ca_2(Al(AlSi)O_7)$. b: Quartz-SiO_2. c: Albite low-$Na(AlSi_3O_8)$. d: Nepheline-$KNa_3Al_4Si_4O_{16}$. e: Anorthite-$CaAl_2Si_2O_8$.)

decrement of heat flux is 61.27 kW m^{-2} for the 443 K case. In consequence, it can be concluded that the decay rates of heat flux with time for the three cases follow the order 443 K > 493 K >543 K.

Nevertheless, the heat flux appears to moderately decay with deposit thickness in stage$_{A-B}$ (stage 2), as illustrated in Figure 10. This stage corresponds to the early sintering process. The sintering process can give rise to neck formation, which will
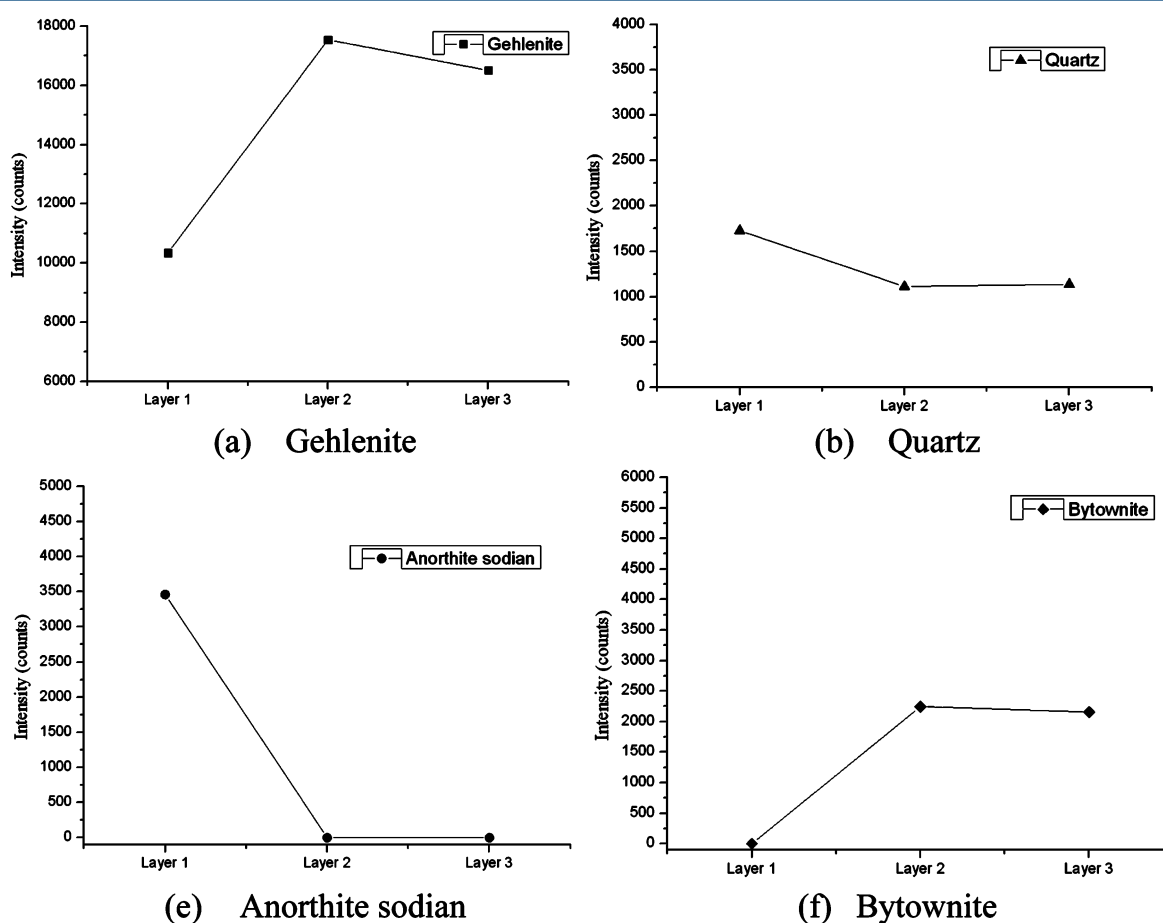
Figure 19. Changes to the main mineral phase of the deposit sample versus layer structure for the 493 K case.

(a) Gehlenite

(b) Quartz

(c) Albite

(d) Anorthite
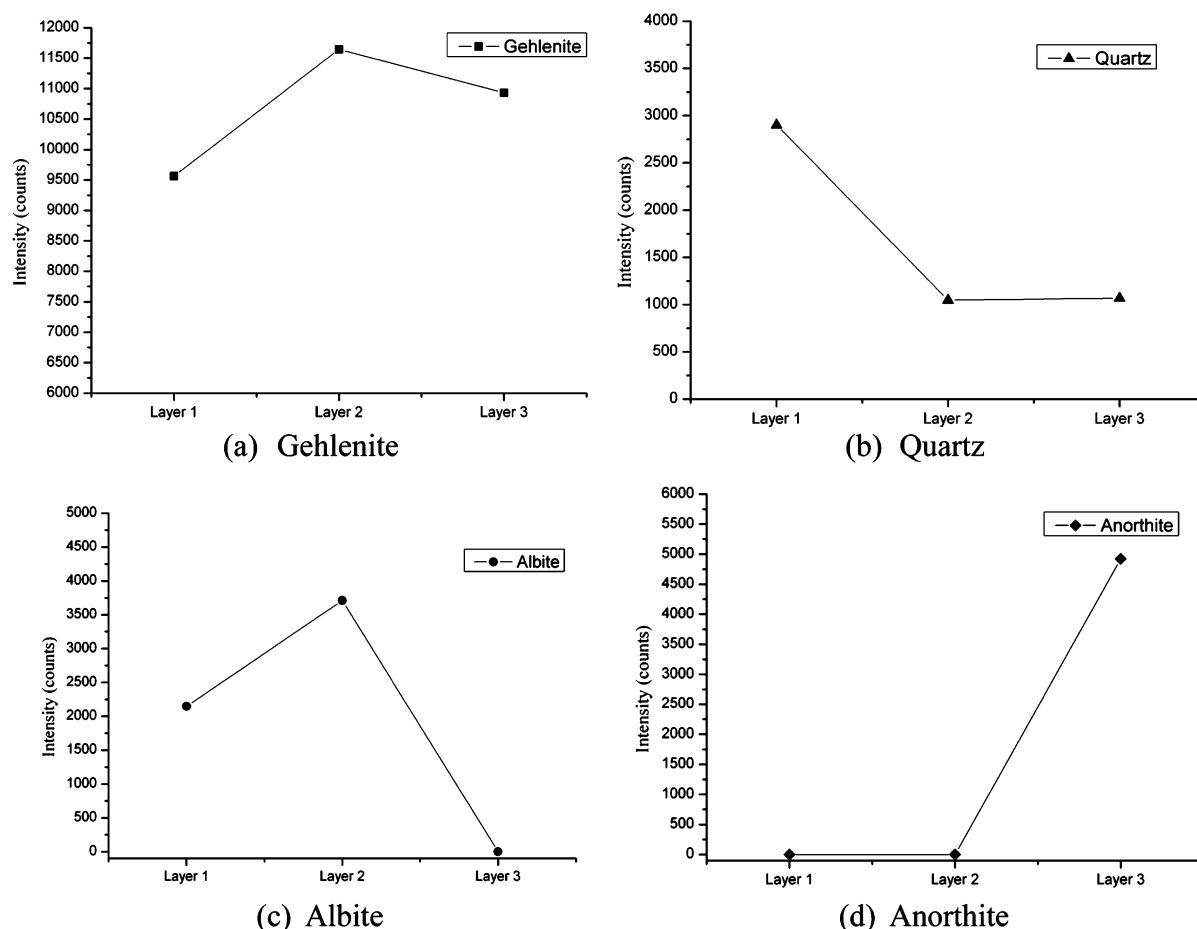
Figure 21. Changes to the main mineral phase of the deposit sample versus layer structure for the 543 K case.

increase contact area between the ash particles. Shrinkage and densification of the deposit particles may occur during the sintering process. Thus, the density and strength of the deposit material will significantly increase after the sintering process. The thermal resistance of this layer is smaller than that of the initial layer. In addition, the fading rate of heat flux in stage 2 is slower that in stage 1. Moreover, for the 543 K case, the increment of deposit thickness is 0.98 mm in stage 2. The duration of this stage is 30 min, and the corresponding decrease in heat flux is 37.47 kW m^{-2}. For the 493 K case, stage 2 lasts 30 min and the deposit thickness increases 1.32 mm. Additionally, the heat flux declines 22.76 kW m^{-2}. For the 443 K case, stage 2 lasts a long time (85 min) and the corresponding attenuation of heat flux is 43.34 kW m^{-2}. The thickness of the deposit increases 3.65 mm. Therefore, the attenuation rates of heat flux with time for the three cases in stage 2 follow this order: 543 K > 493 K >443 K.

Furthermore, stage 3 (stage$_{B-C}$) for the 543 K case lasts 135 min. The corresponding increment of deposit thickness for this stage is 2.08 mm. The decrease in heat flux in this stage is 19.81 kW m^{-2}. For the 493 K case, the duration of stage 3 is 100 min and the corresponding increase in deposit thickness is 2.62 mm. The reduction of heat flux in this stage is 31.16 kW m^{-2}. For the 443 K case, stage 3 lasts 80 min and the corresponding attenuation of heat flux is 7.91 kW m^{-2}. The increment of deposit thickness is 1.71 mm. According to these results, it can be concluded that the attenuation rates of heat flux with time for the three cases in stage 3 follow the order 493 K >543 K >443 K. This stage involves the later sintering process. As the

deposit grows further, the higher surface temperature results in the outer layer of the deposit sintering and even becoming completely molten. Meanwhile, the shrinkage of pores and pore filling by viscous melt flow occur in the stage 3, which result in a remarkable increase in strength and density of the deposit material in the outer layer. In consequence, the heat conductivity of this layer is largest among the three layers. Thus, the attenuation rate of heat flux in this stage is the minimum among the three stages. Moreover, an interesting observation can be made that some data symbols aggregate in an ellipse for all three cases, as illustrated in Figure 10. This is a result of a slight change in both the heat flux and the corresponding deposit thickness at the stable stage; it may be due to the continuous production and rupture of the porosity structure in the deposit at the stable stage.

In addition, it can be found that the stable deposit thicknesses for the 443, 493, and 543 K cases are 6.09−6.20, 4.65−4.76, and 3.47−3.60 mm, respectively. The corresponding stable heat fluxes for the three cases are 48.31, 77.99, and 102.41 kW m^{-2}, respectively. Obviously, it can imply that the stable thickness decreases with the increased deposition surface temperature. As is well-known, when the deposition surface temperature increases, the sintering degree of the deposit will be more serious. At the same time, densification and pore-shrinkage of deposits will occur during the sintering process. In consequence, the stable thickness of the deposit increased with the decreased deposition surface temperature. This result is confirmed by the morphologies of the deposits at the last moment during the experiments for the three cases, as

illustrated in Figure 11. It can be seen that all three deposits present an ellipselike shape on the deposition probe. Nevertheless, the corresponding stable heat fluxes present the opposite tendency, following the order 443 K < 493 K < 543 K. There are two contributing factors to this result: deposit thickness and effective thermal conductivity of deposit. In consequence, the effective thermal conductivity of the three deposits may follow the order 543 K > 493K > 443 K. This conclusion is confirmed by the microstructures of the three deposits; the sintering degree of the outer layer increases with the increased deposition surface temperature. Therefore, the stable heat flux for the 543 K case is the maximum among the three cases.

3.3. Microstructure of the Slagging Deposits. The three slagging deposits were collected and examined by scanning electron microscopy (SEM) equipped with energy dispersive X-ray spectrometry (EDX) to obtain the microstructure and microchemistry of the deposits. First, the slagging deposits were embedded into epoxy resin. Subsequently, the deposits mounted in resin were cut, grinded, and polished to get a smooth cross section. Finally, the cross sections were coated with gold and analyzed by EDX.

The microstructures of the crossed-sectioned deposits are shown in Figures 12, 13, and 14 for the 443, 493, and 543 K cases, respectively. It can be observed that the three deposits are characterized by remarkably different microstructures for different layers. However, the microstructures show no significant relationship with deposition surface temperature. The (a) panels of Figures 12−14 present an overview of layer 1 (initial layer); there are no significant agglomerates, but there is neck formation and some discrete particles are embedded in the epoxy resin. In addition, substantial resin fills the void space between the ash particles. This structure causes the relatively low heat conductivity of the initial layer. This is confirmed by the result illustrated in Figure 10 that the heat flux declines noticeably with deposit thickness in stage$_{O\text{-}A}$. For layer 2 (sintered layer), the epoxy resin area is depleted dramatically and is replaced by a continuous, consolidated particle phase, as shown in the (b) panels of Figures 12−14. In addition, it can be observed that the ash particles are sintered seriously and they are agglomerated to form a more compact morphology. In addition, an abundance of irregular small pores with diameters less than 50 μm are embedded in the sintered layer. The (c) panels of Figures 12−14 exhibit a morphology of layer 3 (slag layer) that is more dense and compact than that of layer 2. Meanwhile, some macro pores with diameters larger than 200 μm distribute in the slag layer.

3.4. Chemical Compositions of the Ash Deposits. The microchemistry of the three slagging deposits is quantitatively examined by EDX analyses. The EDX analysis results are normalized to 100% and given in Table 4 in oxides form. The analysis results reveal that the compositions of the three slagging deposits are dominated by Al, Si, Ca, and Fe, and to a lesser extent, Na, K, Mg, and S. For the 443 K case, it can be observed that the concentrations of Al, Ca, Fe, and Mg increase along the deposit thickness dierection (from layer 1 to layer 3). However, it is not the iron-containing crystalline phase identified by the XRD analysis mentioned in section 3.5. This may be a reason for the reaction of iron oxides with silica forming iron silicates with low melting temperature. In addition, the other elemetns do not display a regular changing trend with the deposit growth direction.

For the 493 K case, it can also be found that the concentrations of Si and Fe increase with the deposit growth direction. Nevertheless, the content of K declines with the deposit thickness direction. It may because the deposit surface temperature increases with the deposit growth, thus the high surface temperature impedes the condensation of K-rich vapors on the surface of the deposit.
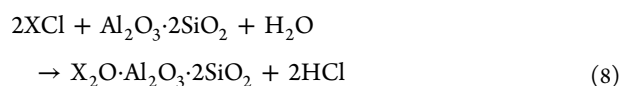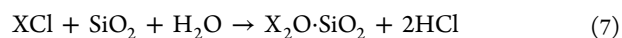
For the 543 K case, the concentrations of Ca increases with the deposit thickness from the inner layer to the outer layer. However, the concentrations of Na, Al, and Si decrease with the thickness direction. An intersting observation can be made that the maximum content of sulfur for the three cases all appear in the initial layer. This may be due to the sulfation of the alkali-based condensates on the probe surface, which is generally temperature-dependent. The initial layer, adjacent to the probe surface, has a temperature lower than that of the other two layers. This can facilitate the condentsation of alkali-rich vapors. Consequently, the initial layer has the maximum content of sulfur in comparison to that of the other two layers.

To get insight into the selective deposition mechanism of each element in the deposit formation, the results of chemical compositions of the three slagging deposits are presented using an enrichment factor (EF), which is the relative enrichment of an element in the collected deposit relative to its content in the coal ash. The enrichment factor EF is defined as

$$\text{EF} = \frac{M_{\text{deposit,i}}}{M_{\text{coal ash,i}}} \tag{6}$$

where $M_{\text{deposit,i}}$ represents the mass fraction of the element i (expressed as oxide) in the deposit and $M_{\text{coal,ash,i}}$ represents the mass fraction of the element i (expressed as oxide) in fuel ash. The corresponding analysis results for the three cases are given in Figure 15.

In Figure 15, it can be observed that the enrichment factors for most elements do not change dramatically between the three cases. Na and K show small EF for all three cases. This implies the alkali metal elements are mobile and generally end up in the gas phase during coal combustion. Subsequently, the alkali-rich species can homogeneously condense on the relative cold deposit probe surface or heterogeneously condense on fly ash particles. The alkali-based components can react with silicates or aluminosilicates to form alkali-rich silicates or aluminosilicates, according to eqs 7 and 8:[24]

$$XCl + SiO_2 + H_2O \rightarrow X_2O \cdot SiO_2 + 2HCl \tag{7}$$

$$2XCl + Al_2O_3 \cdot 2SiO_2 + H_2O$$
$$\rightarrow X_2O \cdot Al_2O_3 \cdot 2SiO_2 + 2HCl \tag{8}$$

where X is Na and/or K. Alkali aluminosilicates or alkali silicates have relatively low melting temperatures, which facilitate the Si−Ca-based fly ash particles sticking on the viscous deposit. The formation of alkali aluminosilicates can also explain why the silicon and aluminum EF are higher than 1 for the three cases, as shown in Figure 15a−c. It can be found that the enrichment factor of SO$_3$ is larger than 1 for all three cases, especially for the initial layer. The enrichment factor of SO$_3$ in the initial layer decreases with increasing deposition surface temperature. As is well-known, alkali-based condensates can react with sulfur-containing compounds to form sulfates, which can be explained by eq 9:

$$2XCl + SO_3 + H_2O \rightarrow X_2SO_4 + 2HCl \tag{9}$$
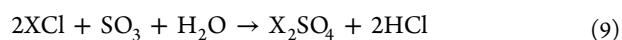
where X represents Na and/or K. In addition, the alkali sulfates are unstable at high temperature, and the condensation reaction is largely dependent on temperature. Consequently, the initial layer of the 443 K case has the highest enrichment factor. Moreover, it can be seen that Al, Si, and Fe EF are higher than 1 for the three cases, except for the enrichment factor of iron for the 543 K case. This suggests that Si, Al, and Fe play an important role in deposit formation. In particular, many aluminosilicates may form in the deposit matrix. Considering XRD analysis results, it can be found that no iron-bearing crystalline phase is identified in the three slagging deposits. In consequence, Fe may exist in terms of iron-bearing silicates or iron-bearing aluminosilicates, which are melted in the glassy phase. This may reuslt from reaction between iron oxide and clay minerals or SiO_2 with fomation of low melting temperature iron-containing aluminosilicates or iron-containing silicates. The involved reactions proceed as

$$FeO + Al_2O_3 \cdot 2SiO_2 \rightarrow FeAl_2Si_2O_8 \tag{10}$$

$$2FeO + 2SiO_2 \rightarrow Fe_2SiO_4 \tag{11}$$
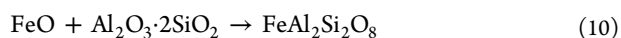
The depsition surface temperature does not significantly affect the enrichment factor of the iron.

3.5. Mineralogy of the Slagging Deposits by XRD Analysis. The crystalline phases of the three slagging deposits collected for the three cases were examined by XRD analysis. Figures 16, 18, and 20 show the XRD patterns of the slagging deposits collected for the 443, 493, and 543 K cases, respectively. The corresponding trends of changes to the main crystalline phases in the three cases are illustrated in Figures 17, 19, and 21. It can be found that the deposition surface temperature did not affect the mineralogy of the deposits significantly. Meanwhile, the results show that the dominant mineral phases of the deposit for the 443 K case are gehlenite, quartz, and bytownite. For the 493 K case, the major components are gehlenite, quartz, sodian anorthite, and bytownite. However, for the 543 K case, the main identified crystalline phases in the deposit are gehlenite, quartz, albite, and anorthite. It can be observed that the most obvious diffraction peak of gehlenite is identified in the sintered layer for the three cases. This suggests that gehlenite is continuously produced with the deposit growth, but part is melted into the amorphous phase in the slag layer because of the high temperature. The formation of gehlenite may result from the reaction between aluminosilicates and the decomposition products of lime stone in coal. The involved reactions can be expressed as

$$CaCO_3 \rightarrow CaO + CO_2 \tag{12}$$

$$2CaO + Al_2O_3 \cdot SiO_2 \rightarrow Ca_2(Al(AlSi)O_7) \tag{13}$$
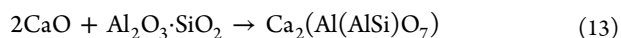
The bytownite and sodian-anorthite mineral phases can be referred to as derivatives of anorthite, which may result from the reaction between alkali-rich condensates and Si−Al-containing fly ashes. The mechanism is similar to that shown in eq 8. The occurrence of diopside implies the reaction of anorthite with magnesium oxide and iron oxide.

For the 493 K case, the absence of sodian anorthite in the sintered layer and slag layer in contrast to the occurrence of bytownite in these two layers, which indicates that sodian anorthite can transform into bytownite. For the 543 K case, the occurrence of albite may reuslt from the reaction of alkali-based condensates with aluminosilicates. The anorthite mineral phase exists only in the slag layer. This suggests that anorthite has a

relatively high melting temperature. Acccording to Unsworth et al.,[25] the anorthite mineral phase is formed by the solid-state reaction rather than the crystallizaion of a homogeneous melt. The involved reaction is expressed as

$$CaO + Al_2O_3 \cdot 2SiO_2 \rightarrow CaAl_2Si_2O_8 \tag{14}$$
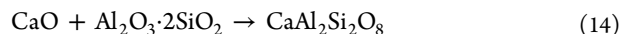
When this is combined with the depletion of gehlenite in the slag layer, it can be concluded that some anorthite phases may result from the transformation of gehlenite:[26]

$$Ca_2(Al(AlSi)O_7) + Al_2O_3 + 3SiO_2 \rightarrow 2CaAl_2Si_2O_8 \tag{15}$$
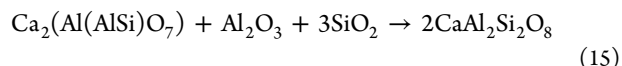
In addition, it can be found that the deposition surface temperature has significant effect on the formation of gehlenite, as shown in Figures 17a, 19a, and 21a. This shows that intensity of gehlenite for the three cases follows the order 493 K > 543 K > 443 K. This result reveals that the formation of gehlenite requires a high temperature, but too of a high temperature will impede the formation of this mineral phase.

4. CONCLUSIONS

To study the effect of deposition surface temperature on the slagging characteristics, three slagging tests have been conducted in a pilot scale furnace. In addition, the inlet temperature of cooling oil was set as 443, 493, and 543 K for the three tests. A digital image technique has been used to monitor the deposit morphology online. A clear relationship between the deposition rates, deposit microstructure, chemical composition, and deposition surface temperature has been found. The following conclusions can be drawn: (1) The deposition surface temperature has an evident effect on the deposition rates and morphology. The sintering degree of the deposit surface increases with the increasing deposition surface temperature. The growth rates of the ash deposit's four stages are 0.069, 0.035, 0.011, and 0 mm/min, corresponding to stages 1, 2, 3, and 4, respectively, for the 443 K case. The growth rates of the deposit for the 493 K case are 0.048, 0.030, 0.007, and 0 mm/min, corresponding to stages 1, 2, 3, and 4, respectively. However, for the 543 K case, the growth rates of the deposit are 0.032, 0.025, 0.011, and 0 mm/min, corresponding to stages 1, 2, 3, and 4, respectively. The stable thickness of the three deposits can be kept to 6.09−6.20, 4.65−4.76, and 3.47−3.60 mm for the 443, 493, 543 K cases, respectively. This result reveals that the stable thickness decreases with the increased deposition surface temperature. (2) The SEM images show that the deposition surface temperature has an effect on the microstructure of the deposit, especially for the slag layer of the deposit. The results show that the higher deposition surface temperature will give rise to the occurrence of a more compact morphology and more macro pores in the slag layer. The low deposition surface temperature can facilitate the formation of sulfates in the initial layer. In addition, the results show that the dominant mineral phases of the deposit for the 443 K case are gehlenite, quartz, and bytownite. For the 493 K case, the major components are gehlenite, quartz, sodian anorthite, and bytownite. For the 543 K case, the main identified crystalline phase in the deposit are gehlenite, quartz, albite, and anorthite. The deposition surface temperature mainly affects the concentration of gehlenite in the deposits. In addition, the content of every crystalline phase changes noticeably along the deposit growth direction for each case.

■ AUTHOR INFORMATION

Corresponding Author

*Tel.: +86-571-87952598. Fax: +86-571-87951616. E-mail: zhouhao@cmee.zju.edu.cn.

Notes

The authors declare no competing financial interest.

■ REFERENCES

(1) Vuthaluru, H. B.; French, D. Ash chemistry and mineralogy of an Indonesian coal during combustion: Part II — Pilot scale observations. *Fuel Process. Technol.* **2008**, *89*, 608–621.

(2) Shimogori, M.; Mine, T.; Ohyatsu, N.; Takarayama, N.; Matsumura, Y. Effects of fine ash particles and alkali metals on ash deposition characteristics at the initial stage of ash deposition determined in 1.5 MW_th pilot plant tests. *Fuel* **2012**, *97*, 233–240.

(3) Yoshiie, R.; Tsuzuki, T.; Ueki, Y.; Nunome, Y.; Naruse, I.; Sato, N.; et al. Effects of coal types on ash fragmentation and coalescence behaviors in pulverized coal combustion. *Proc. Combust. Inst.* **2013**, *34*, 2895–2902.

(4) Vamvuka, D.; Mistakidou, E.; Drakonaki, S.; Foscolos, A.; Kavouridis, K. Ash Quality of a Beneficiated Lignite from Ptolemais Basin, Northern Greece. *Energy Fuels* **2001**, *15*, 1181–1185.

(5) Richards, G. H.; Slater, P. N.; Harb, J. N. Simulation of Ash Deposit Growth in Pulverized Coal-Fired Pilot Scale Reactor. *Energy Fuels* **1993**, *7*, 774–781.

(6) Arvelakis, S.; Folkedahl, B.; Johansen, K. D.; Hurley, J. Studying the Melting Behavior of Coal, Biomass, and Coal/Biomass Ash Using Viscosity and Heated Stage XRD Data. *Energy Fuels* **2006**, *20*, 1329–1340.

(7) Kostakis, G. Mineralogical composition of boiler fouling and slagging deposits and their relation to fly ashes: The case of Kardia power plant. *J. Hazard. Mater.* **2011**, *185*, 1012–1018.

(8) Wang, H.; Harb, J. N. Modeling of ash deposition in large-scale combustion facilities burning pulverized coal. *Prog. Energy Combust. Sci.* **1997**, *23*, 267–282.

(9) Ma, Z.; Iman, F.; Lu, P.; Sears, R.; Kong, L.; Rokanuzzaman, A. S.; McCollor, D. P.; Benson, S. A. A comprehensive slagging and fouling prediction tool for coal-fired boilers and its validation/application. *Fuel Process. Technol.* **2007**, *88*, 1035–1043.

(10) Naruse, I.; Kamihashira, D.; Khairil; Miyauchi, Y.; Kato, Y.; Yamashita, T.; Tominaga, H. Fundamental ash deposition characteristics in pulverized coal reaction under high temperature conditions. *Fuel* **2005**, *84*, 405–410.

(11) Zbogar, A.; Frandsen, F.; Jensen, P. A.; Glarborg, P. Shedding of ash deposits. *Prog. Energy Combust. Sci.* **2009**, *35*, 31–56.

(12) Tomeczek, J.; Waclawiak, K. Two-dimensional modeling of deposits formation on platen superheaters in pulverized coal boilers. *Fuel* **2009**, *88*, 1466–1471.

(13) Ni, J.; Zhou, Z.; Yu, G.; Liang, Q.; Wang, F. Molten Slag Flow and Phase Transformation Behaviors in a Slagging Entrained-Flow Coal Gasifier. *Ind. Eng. Chem. Res.* **2010**, *49*, 12302–12310.

(14) Waclawiak, K.; Kalisz, S. A practical numerical approach for prediction of particulate fouling in PC boilers. *Fuel* **2012**, *97*, 38–48.

(15) Rushdi, A.; Gupta, R.; Sharma, A.; Holcombe, D. Mechanistic prediction of ash deposition in a pilot-scale test facility. *Fuel* **2005**, *84*, 1246–1258.

(16) Wang, X.; Liu, Y.; Tan, H.; Ma, L.; Xu, T. Mechanism Research on the Development of Ash Deposits on the Heating Surface of Biomass Furnaces. *Ind. Eng. Chem. Res.* **2012**, *51*, 12984–12992.

(17) Mu, L.; Zhao, L.; Liu, L.; Yin, H. Elemental Distribution and Mineralogical Composition of Ash Deposits in a Large-Scale Wastewater Incineration Plant: A Case Study. *Ind. Eng. Chem. Res.* **2012**, *51*, 8684–8694.

(18) Alvarez, R.; Callén, M. S.; Clemente, C.; Díaz-Bautista, M. A.; López, J. M.; Mastral, A. M.; Murillo, R. Slagging in Fluidized Bed Combustion of Rubber Tire. Inorganic Component Evolution. *Ind. Eng. Chem. Res.* **2004**, *43*, 7762–7767.

(19) Mischa, T.; Bengt, J. S.; Maria, Z.; Mikko, H.; Honghi, T. Fouling tendency of ash resulting from buring mixtures of biofuel. Part 3. Influence of probe surface temperature. *Fuel* **2006**, *85*, 2002–2011.

(20) Akiyama, K.; Pak, H.; Tada, T.; Ueki, Y.; Yoshiie, R.; Naruse, I. Ash Deposition Behavior of Upgraded Brown Coal and Bituminous Coal. *Energy Fuels* **2010**, *24*, 4138–4143.

(21) Kupka, T.; Zajac, K.; Weber, R. Effect of Fuel Type and Deposition Surface Temperature on the Growth and Structure of an Ash Deposit Collected during Co-firing of Coal with Sewage Sludge and Sawdust. *Energy Fuels* **2009**, *23*, 3429–3436.

(22) Zhou, H.; Zhou, B.; Qu, H.; Lin, A.; Cen, K. Experimental Investigation of the Growth of Ash Deposits with and without Additives through a Digital Image Technique. *Energy Fuels* **2012**, *26*, 6824–6833.

(23) Zhou, H.; Zhou, B.; Dong, K.; Ding, J.; Cen, K. Research on the slagging characteristics of easy to slagging coal in a pilot scale furnace. *Fuel* **2013**, *109*, 608–615.

(24) Niu, Y.; Tan, H.; Ma, L.; Pourkashanian, M.; Liu, Z.; Liu, Y.; Wang, X.; Liu, H.; Xu, T. Slagging characteristics on the supperheaters of a 12 MW biomass-fired boiler. *Energy Fuels* **2010**, *24*, 5222–5227.

(25) Unsworth, J. F.; Barratt, D. J.; Park, D.; Titchener, K. J. Ash formation during pulverized coal combustion: 2. The significance of crystalline anorthite in boiler deposits. *Fuel* **1988**, *67*, 632–641.

(26) Traoré, K.; Kabrè, T. S.; Blanchart, P. Low temperature sintering of a pottery clay from Burkina Faso. *Appl. Clay Sci.* **2000**, *17*, 279–292.

7246

dx.doi.org/10.1021/ie4041516 | *Ind. Eng. Chem. Res.* 2014, 53, 7233–7246